



Final Draft

of the original manuscript

Shi, S.; Li, Y.; Ngo-Dinh, B.; Markmann, J.; Weissmüller, J.:
**Scaling behavior of stiffness and strength of hierarchical
network nanomaterials.**

In: Science. Vol. 371 (2021) 6533, 1026 – 1033.

First published online by AAAS: 05.03.2021.

<https://dx.doi.org/10.1126/science.abd9391>

Scaling behavior of stiffness and strength of hierarchical network nanomaterials

Shan Shi^{1,2*}, Yong Li^{1,2}, Bao-Nam Ngo-Dinh^{1,3}, Jürgen Markmann^{1,2}, Jörg Weissmüller^{1,2*}

Structural hierarchy can enhance the mechanical behavior of materials and systems. This is exemplified by the fracture toughness of nacre or enamel in nature and by human-made architected microscale network structures. Nanoscale structuring promises further strengthening, yet macroscopic bodies built this way contain an immense number of struts, calling for scalable preparation schemes. In this work, we demonstrated macroscopic hierarchical network nanomaterials made by the self-organization processes of dealloying. Their hierarchical architecture affords enhanced strength and stiffness at a given solid fraction, and it enables reduced solid fractions by dealloying. Scaling laws for the mechanics and atomistic simulation support the observations. Because they expose the systematic benefits of hierarchical structuring in nanoscale network structures, our materials may serve as prototypes for future lightweight structural materials.

Hierarchical structures, featuring several relevant length scales, are common in nature, engineering, and society. Often, the hierarchy is motivated by optimizing function—for instance, the transport of fluids (1–3) or vehicles (4). Another prominent use of hierarchy is in optimizing mechanical behavior while satisfying boundary conditions on material class, mass density, or manufacturing costs. Nature is well known to exploit hierarchy for optimizing fracture toughness in nacre, bone, and enamel (5–9). Strong and lightweight hierarchical truss structures at the macroscale have been used for more than a century (10). By exploiting modern three-dimensional (3D) manufacturing techniques, this approach has been transferred to the microscale. Architected truss structures have been demonstrated with extremely low density, high specific strength, and high resilience [(11–15); for a comprehensive review, see (16)].

Driving the size of architected truss structures into the regime of nanometers has been recognized as beneficial (13, 16, 17) because this exploits the high strength of metal nanostructures (18). Using struts of 10 nm in dimension would imply on the order of 10^{14} struts in a cubic millimeter. Rather than 3D manufacturing, producing that many microstructural elements requires the self-organized processes that are characteristic of microstructure evolution in materials science. In other words, making truly nanoscale open-network structures by materials preparation routes that are scalable and so yield macroscopic bodies is an area of high interest. Micrometer-scale microstructures made by

spinodal decomposition or colloidal crystallization may act as templates for thin shells to provide macroscopic bodies in which one dimension—the shell thickness—is in the nanoscale (19–21). Yet, although such approaches exemplify the versatility of nature's self-organization processes, they have yet to achieve structural hierarchy. Various routes can lead to hierarchy in nanoporous metals (22, 23), yet homogeneous macroscopic bodies are the exception, and interesting mechanical properties remain to be demonstrated for this class of materials.

Network nanomaterials with a single characteristic size have been demonstrated on the basis of dealloying (24). In this process, corrosion removes one constituent from a solid solution, and the remaining constituent reorganizes to form an open-network material. Dealloying can produce homogeneous monolithic bodies that are millimeters or centimeters in size (25–27), whereas strut sizes reach down to a few nanometers (28). These bodies are deformable to large plastic strain without failure, and their effective macroscopic strength is consistent with the extremely high local strength of the nanoscale struts (29–33). Dealloying is best understood as a process for nanoporous gold (NPG), but protocols for lighter and stronger metals, such as Ti, Al, and high-entropy alloys, are becoming available (34–37).

Dealloying is also a pathway to hierarchical network materials and specifically to structures with a particularly stringent architecture in the form of two geometrically similar networks that are nested on two well-defined, distinctly different length scales (38–40). However, macrodefects have impaired investigations of the mechanical behavior of these materials.

Dealloying can provide solid volume fractions, φ , down to ~ 0.25 in single length-scale networks. Reducing φ requires increasing the aspect ratio of the struts, yet long and thin

struts tend to be Plateau-Rayleigh instable (33, 41, 42). This problem is generally relevant for nanomaterials, and it applies specifically for metallic nanostructures that emerge from diffusion-driven self-organization, which is the active process during dealloying. Consequently, the connectivity of dealloying-made network materials deteriorates when φ falls below ~ 0.3 , and so do stiffness and strength (43). This observation provides an incentive for hierarchical nanoscale network materials. To reach low φ in a stable structure, short and thick struts on any given hierarchy level can be built as a network made of a set of much smaller struts, which are also short and thick (and thus stable) on a lower structural hierarchy level. In this way, self-organized (and thus scalable) processes may be expected to build low-density (and thus lightweight) nanoscale (and thus strong) networks with good connectivity and high strength and stiffness.

We report a dealloying route toward the scalable and controllable preparation of macroscopic monolithic bodies of nested-network nanoporous gold (N³PG) that are free of macrodefects. The characteristic size at the lower hierarchy level is as small as 15 nm, and φ can be as low as 0.12. This value has been very challenging to attain in nanoscale network materials made by dealloying. Macroscale compression tests show that the stiffness and strength increase when going from the single scale to the hierarchical material. Our findings are explained by scaling laws that emerge from recursive homogenization approaches on the individual hierarchy levels, and we corroborated them using molecular dynamics (MD) simulation of the mechanical behavior.

Preparing nested-network nanomaterials

Our monolithic N³PG samples were made by a refined variant of the “dealloying-coarsening-dealloying” protocol (Fig. 1A) (39, 44). Our preparation goes through three stages, an as-dealloyed nanoporous Ag-Au (stage i), a coarsened nanoporous Ag-Au (stage ii), and N³PG (stage iii). Stage i is generated when the Ag₉₃Au₇ master alloy is electrochemically dealloyed in 0.01 M H₂SO₄. During this process, nanoporous Ag-Au forms by surface diffusion as the Ag is partially dissolved. Stage ii is obtained by coarsening the stage i material through a vacuum anneal. This establishes the structure of the upper hierarchy level. The final, stage iii hierarchical material is obtained when the residual Ag is removed during a second electrochemical dealloying process in 1.0 M HClO₄. This process creates a much smaller porous structure inside the larger struts of the coarsened stage ii material. The smaller structure represents the lower hierarchy level.

Scanning electron microscopy (SEM) images of the stage i material (Fig. 1B) exhibit the

¹Institute of Materials Research, Materials Mechanics, Helmholtz Zentrum Geesthacht, 21502 Geesthacht, Germany.

²Institute of Materials Physics and Technology, Hamburg University of Technology, 21073 Hamburg, Germany.

³Institute for Materials, Technical University of Braunschweig, 38106 Braunschweig, Germany.

*Corresponding author. Email: shan.shi@hzg.de (S.S.); weissmueller@tuhh.de (J.W.)

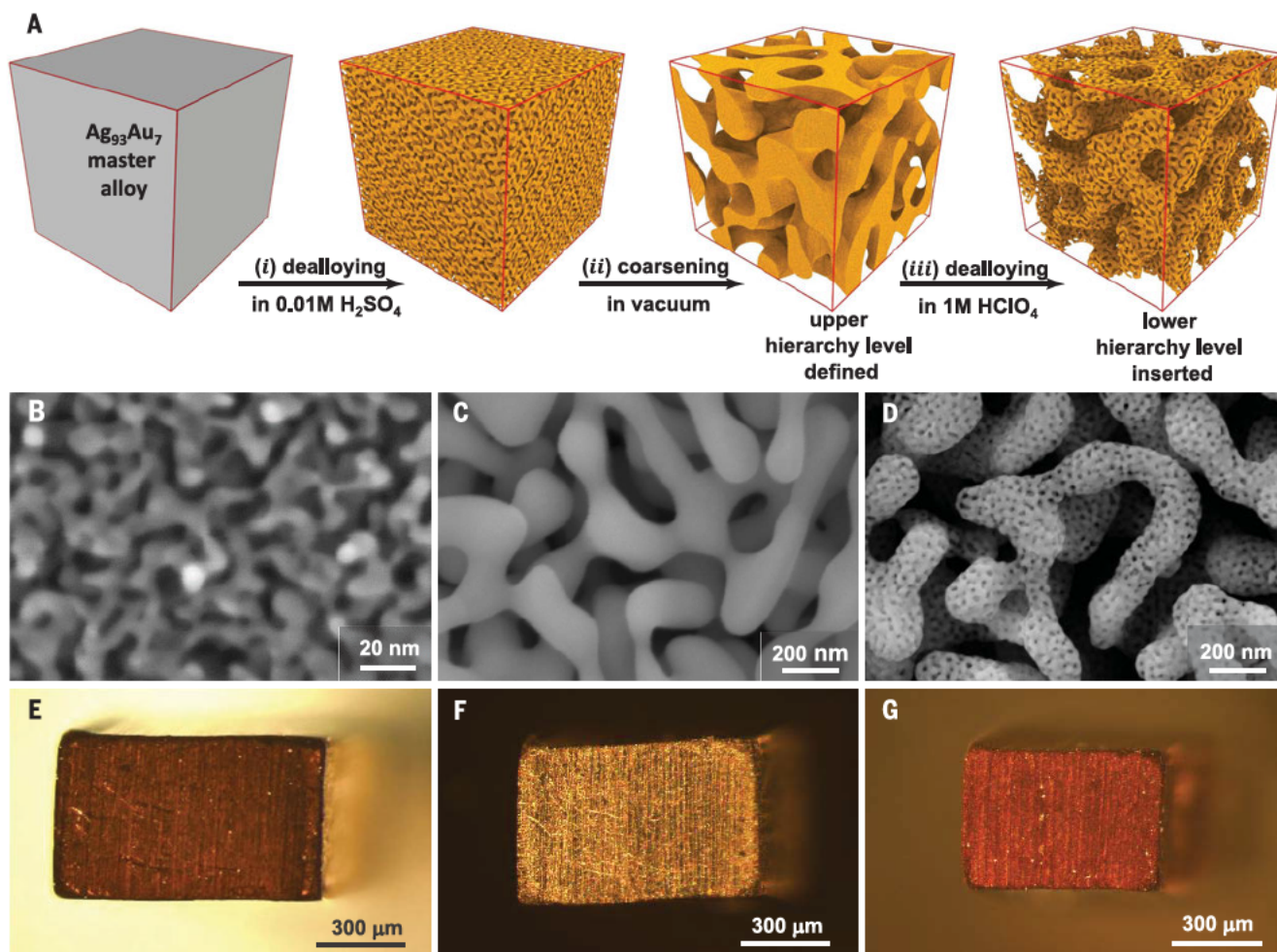


Fig. 1. Fabrication and microstructure characterization of N³PG.

(A) Schematic describing the synthesis route of monolithic, crack-free N³PG. Stage i: Electrochemical dealloying of Ag₉₃Au₇ master alloy in 0.01 M H₂SO₄ aqueous electrolyte creates a monomodal bicontinuous porous structure and remains a substantial amount of Ag. Stage ii: Annealing as-dealloyed nanoporous Ag-Au alloy in vacuum leads to coarser microstructure (see much larger solid strut and pore size). Stage iii: A second electrochemical dealloying process on

coarsened nanoporous Ag-Au alloy in 1.0 M HClO₄ substantially dissolves residual Ag and creates bicontinuous porous structure inside the solid strut. (B to D) SEM images showing fracture surface microstructure of (B) as-dealloyed nanoporous Ag₇₆Au₂₄, (C) coarsened nanoporous Ag₇₆Au₂₄ (400°C for 30 min), and (D) as-prepared N³PG. (E to G) Optical microscope images showing crack-free overview of (E) as-dealloyed nanoporous Ag₇₆Au₂₄, (F) coarsened nanoporous Ag₇₆Au₂₄ (400°C for 30 min), and (G) as-prepared N³PG.

characteristic network structure of dealloying. The strut size, defined as the mean strut diameter, is as low as $L = 7$ nm. In stage ii (Fig. 1C), the Ag-Au alloy of stage i has coarsened to the larger strut size of $L = 110$ nm, whereas the microstructure appears geometrically similar to that of stage i. We found, using energy-dispersive x-ray spectroscopy (EDX), a Ag atom fraction, x_{Ag} , of 76%. The hierarchical nested-network nanostructure of the stage iii material appears after the second dealloying (Fig. 1D). The struts of stage ii acquired an internal porosity after the second dealloying, and two well-defined strut sizes of $L_1 = 15$ nm and $L_2 = 110$ nm form the lower and upper hierarchy levels, respectively. The size of L_2 is close to L at stage ii. Our EDX measurements suggest that $x_{Ag} < 5$ atomic % (at %) in stage iii samples. Samples

with these characteristics could be reproducibly made and mechanically tested.

Optical images suggest that the samples are monolithic and free of macroscale cracks (Fig. 1, E to G). The smaller dimensions of the stage iii sample indicate shrinkage during the second dealloying. The net volumetric shrinkage during the entire preparation is 48%, substantially less than previously reported (39). By using SEM on fracture surfaces, we found that the nested-network nanostructure (Fig. 1D) is perfectly uniform throughout the bulk of millimeter-sized samples (Fig. 1G).

We recognized that the careful selection of electrolyte and dealloying potential at stage i is decisive for making homogeneous monolithic samples. As compared with the standard electrolyte, 1.0 M HClO₄, we achieved superior

retention of Ag with 0.01 M H₂SO₄. We speculate that this is related to the high surface diffusivity of Au in H₂SO₄ (45), which promotes passivation and hence the burying of Ag within the stage i struts. Furthermore, working only slightly above the critical dealloying potential (0.359 V), as determined from the polarization plot (fig. S1), at stage i enabled dealloying throughout the bulk with little shrinkage. The residual Ag varies between 79 and 69 at % in the very small interval of dealloying potentials, 0.359 to 0.368 V (fig. S2). This range is above the parting limit, 55 at % Ag (46), which affords complete dealloying at stage iii.

By tuning the preparation conditions, the microstructure parameters of our nested-network materials can be varied. We focused

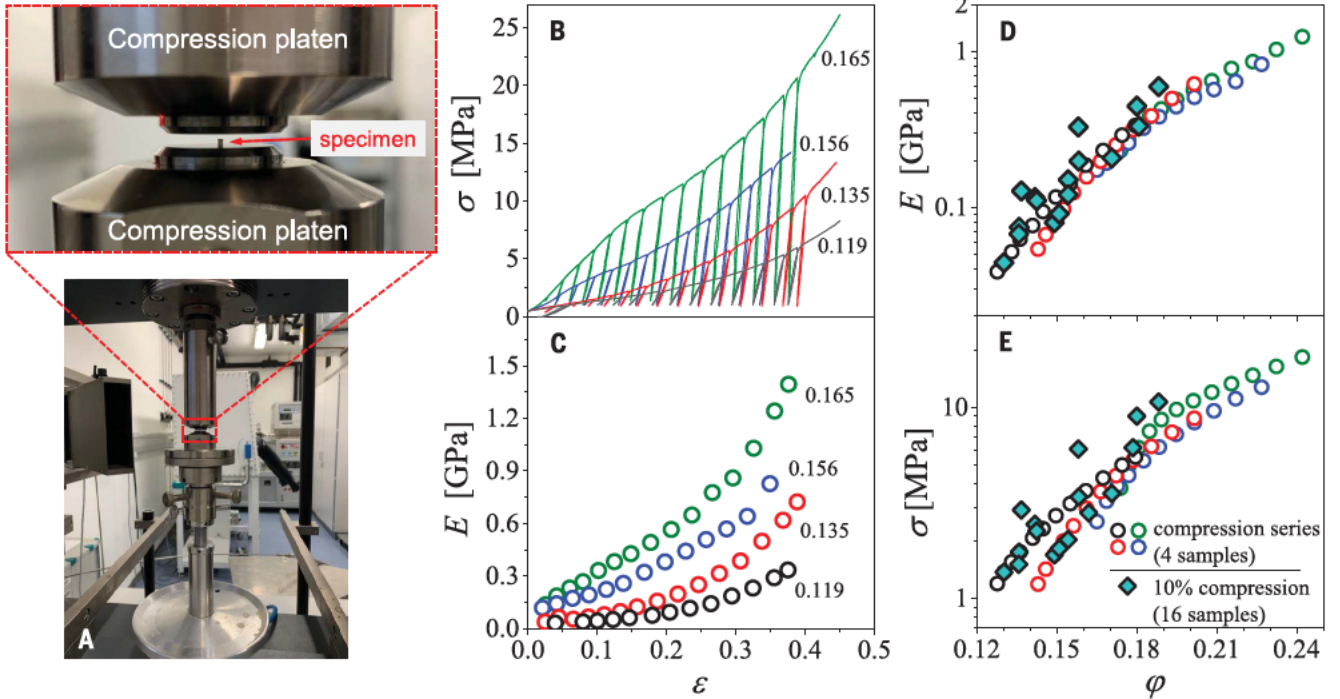


Fig. 2. Uniaxial macrocompression on N³PG with various solid fractions.

(A) Photograph of a conventional macroscale testing device for compression tests. Partial enlarged figure (top) shows a millimeter-sized specimen on the compression platen. (B) Engineering stress-strain (σ vs ϵ) curves, including unload-and-reload segments for N³PG with initial solid fraction (ϕ) ranging

from 0.119 to 0.165. (C) Effective Young's modulus (E) versus ϵ during compression. (D to E) E and σ versus ϕ . Solid symbols, 16 individual samples at 10% strain. Open symbols, the four individual samples from (B), with ϕ varying from 0 to 30% during the compression series. Labels in (B) and (C) specify initial ϕ .

on two series of samples. In the first series, we varied the initial (of the as-prepared stage iii material before deformation) value of the overall ϕ by adjusting the dealloying potential in the interval 0.359 to 0.368 V at stage i while the strut sizes remained constant. In the second series, we varied L_2 by adjusting the stage ii annealing conditions.

Impact of solid fraction on Young's modulus and strength

We explored the mechanical behavior of N³PG samples with similar strut sizes, $L_1 = 15$ nm and $L_2 = 110$ nm, but different initial ϕ . We conducted our uniaxial compression tests on the millimeter-sized samples using a conventional mechanical testing device (Fig. 2A).

We measured engineering stress-strain curves with unload-and-reload segments for N³PG with initial ϕ in the range of 0.119 to 0.165 (Fig. 2B). All samples can be deformed to large strain without failure. Pronounced and continuously increasing strain hardening is apparent, suggesting homogeneous plastic deformation. We determined the effective Young's modulus (E) as the secant modulus of unload-and-reload segments during plastic deformation (Fig. 2C). Samples with higher initial ϕ are stiffer, and E increases with increasing plastic strain.

We have followed the variation of E and the effective, macroscopic strength (σ) as ϕ is varied (i) by densification during deformation for one and the same sample or (ii) by preparation for separate samples predeformed identically (to 10% plastic strain). All data agree well (Fig. 2, D and E), supporting the reproducibility of our preparation protocol as well as the homogeneity of the millimeter-size monoliths. Furthermore, the consistency suggests that, within the restricted regime of solid fractions studied in this work, ϕ is an appropriate descriptor of the material, irrespective of whether ϕ was established by tuning the preparation conditions or by imposing plastic deformation.

We compare the E of hierarchical N³PG with experimental data from the literature for as-prepared NPG with a single length scale (Fig. 3). The known consistency of the experimental literature data is apparent (Fig. 3A). The figure includes finite-element simulation data (43) for E of spinodal and self-organized nanoscale network structures with a single hierarchy level. Those simulation data extend the range of solid fractions downward. The combination of experiment and simulation illustrates the established (33, 43) pronounced drop of the stiffness of network materials formed by dealloying for ϕ substantially below

0.3. At such low ϕ , our hierarchical samples appear substantially stiffer than the trends suggested from the nonhierarchical ones. Furthermore, the hierarchical samples extend the range of solid fractions accessible to dealloyed network materials to substantially lower values.

The Gibson-Ashby scaling law for E (eq. S2) approximates the scaling for some of the architected lattice structures (fig. S4C). The lesser E at low ϕ in our data arises from the loss in connectivity when going from geometrically optimized architected structures with a restricted number of struts to scalable network materials made by nanoscale self-organization. The architected structures with ϕ comparable to our material exhibit $<10^4$ struts, orders of magnitude below the 10^{12} struts (44) of our N³PG samples.

We determined the effective, macroscopic strength versus the solid fraction (Fig. 3B). We normalized the strength to the value at the strut level, σ_0 , which is size dependent. We adopted the values in (47) for this dependency. All of our samples have a sensibly identical lower-level strut size, $L_1 = 15$ nm. We estimated the value of σ_0 at that size to be 2.3 GPa (47). As we found for the stiffness, the data for the strength of nonhierarchical NPG from different literature sources (44) are quite

consistent, and the hierarchical material explores a range of solid fractions that are substantially below those of the nonhierarchical material.

Scaling laws for Young's modulus and strength

Our discussion of scaling laws adopts the suggestion of a recursive homogenization scheme for modeling the mechanical behavior of hierarchical structures or materials (6, 10). When applied to nested networks, the underlying assumption is that the effective (homogenized) value, P_{eff} , of the mechanical materials property P at any hierarchy level j of the network can be understood as the product of the local value, P_{loc} , of P in the struts at that level and of a function p that depends on the geometry of the microstructure, in the simplest case through the strut volume fraction, φ_j , at the respective level. Because P_{loc} embodies the effective material's behavior at the next lower hierarchy level, one obtains the recursive formula and the result for the net value, P_{net} , of P as

$$P_{\text{eff}j} = P_{\text{eff}j-1} p(\varphi_j) \quad (1)$$

$$P_{\text{net}} = P_0 \prod_{j=1}^n p(\varphi_j) \quad (2)$$

for a material with n hierarchy levels. P_0 is the local value of P in the massive material that forms the elementary structural units (in this work, the struts) at the lowest hierarchy level.

Often, the P_{eff} depend on φ by a power law, so that $P_{\text{eff}} = b P_{\text{loc}} \varphi^\beta$ with b and β constants. Consider, for simplicity, a "strong" self-similarity, characterized by a common value, $\bar{\varphi}$, of the solid fraction at each of the n hierarchy levels. The net values of the solid fraction and of P are then $\varphi_{\text{net}} = \bar{\varphi}^n$ and (by Eq. 2) $P_{\text{net}} = P_0 b^n \varphi_{\text{net}}^\beta$, respectively. As has been pointed out (10), the impact of hierarchical structuring on the mechanics is here simply represented by the factor b^n . Hierarchy then has no impact on the mechanics if $b = 1$, as for Young's modulus of foams, and it will lead to a progressive deterioration of the behavior if $b < 1$, as for the strength of foams (10, 48).

Power-law scaling is well established for materials with a macroscale microstructure, such as conventional foams (48). Yet power laws may generally not be expected for materials in which a nanoscale bicontinuous microstructure forms by self-organization. Nanoscale struts with a high aspect ratio, required for low φ , tend to disconnect because of the Plateau-Rayleigh instability (33, 41, 42). The result is a progressive loss of connectivity in the network as φ decreases, abutting in a percolation threshold at a finite value, φ_{per} , of the solid fraction. A modified Roberts-Garbozci

law has been proposed for the mechanical behavior of such materials. Limited to not-too-large φ , this law takes the form (43)

$$P_{\text{eff}} = P_{\text{loc}} C \left(\frac{\varphi - \varphi_{\text{per}}}{1 - \varphi_{\text{per}}} \right)^m \quad (3)$$

with C and m constants.

For the effective E of bicontinuous materials formed by spinodal decomposition or dealloying and for $\varphi \leq 0.5$, the constants in Eq. 3 take the values $\varphi_{\text{per}} \approx 0.16$, $C \approx 2$, and $m \approx 5/2$. Because the predicted values of E agree well with experimental data for as-prepared dealloyed NPG (43), we explored the ramifications of Eq. 3 for N³PG. Combining the scaling law with the recursive homogenization scheme of Eq. 2 and assuming strong self-similarity, we obtained for the net effective Young's modulus

$$E_{\text{net}} = E_0 2^n \left(\frac{\varphi_{\text{net}}^{1/n} - \varphi_{\text{per}}}{1 - \varphi_{\text{per}}} \right)^{5n/2} \quad (4)$$

for $\varphi_{\text{net}} \leq 2^{-n}$.

Experiment provides strong evidence for a systematic correlation between the stiffness and strength of nanoscale metal network materials made by dealloying (47, 49). The underlying notions are that (i) disconnected

regions of the network will contribute to the solid fraction but, because they bear no load, not to the effective mechanical behavior and that (ii) the Gibson-Ashby scaling relations for open-cell foams (Fig. 3) apply to the well-connected, load-bearing part of the material. These findings can be combined with the modified Roberts-Garbozci law for E to obtain a tentative scaling law for the strength of NPG, accounting for the percolation threshold (44). For $\varphi \leq 0.5$, this law again takes the form of Eq. 3, but with the modified parameters $C \approx 1/2$ and $m \approx 15/8$ (eq. S6). The estimated value of m agrees well with the empirical value, $m = 1.84$ (49), obtained by fitting experimental strength data for dealloyed nanoporous Fe-Cr with Eq. 3. Combining this scaling law with Eq. 2, we obtained the yield strength of the hierarchical material as

$$\sigma_{\text{net}} = \sigma_0 \frac{1}{2^n} \left(\frac{\varphi_{\text{net}}^{1/n} - \varphi_{\text{per}}}{1 - \varphi_{\text{per}}} \right)^{15n/8} \quad (5)$$

for $\varphi_{\text{net}} < 2^{-n}$. The scenario underlying Eqs. 4 and 5 of strong self-similarity (identical φ at each hierarchy level) provides the optimum stiffness and strength for a given φ_{net} (44).

We used Eqs. 4 and 5 to predict the variations of stiffness and strength with the φ in structures with different numbers of hierarchy

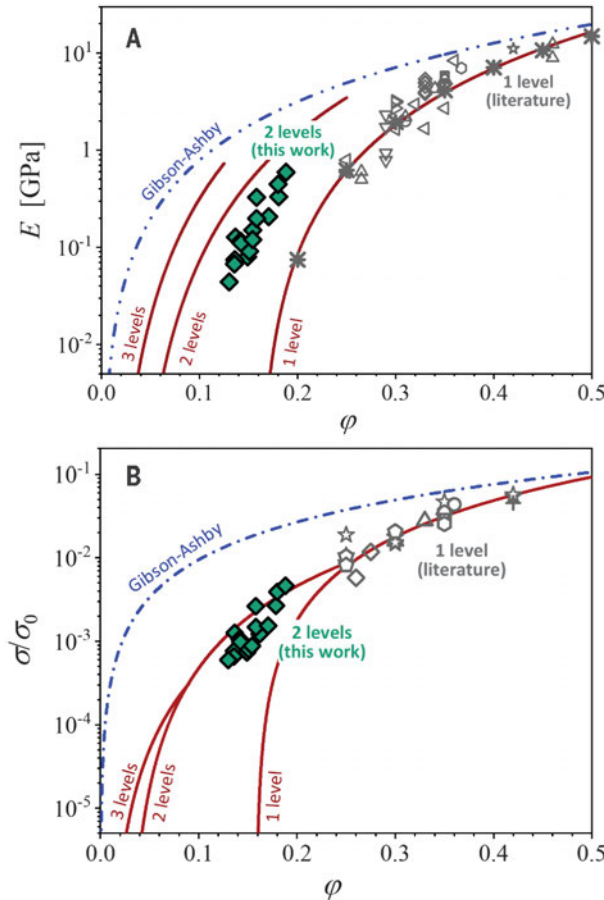


Fig. 3. Scaling behavior of stiffness and strength with solid fraction for NPG with different numbers of hierarchy levels. (A) Effective Young's modulus (E) versus solid fraction (φ). **(B)** Normalized yield strength (σ/σ_0) versus φ . σ_0 denotes local strut strength at the lowest hierarchical level (47). Solid symbols, experimental N³PG ($n = 2$). Open symbols, literature data for experimental nonhierarchical NPG ($n = 1$) taken from various sources [for details and a version with log-log axis scaling, see fig. S4 (44)]. Asterisks, simulated data of spinodal and self-organized nanoscale network structures with a single hierarchy level ($n = 1$) (43). Lines, theory recursive homogenization, Eqs. 4 and 5; broken lines, Gibson-Ashby laws (44).

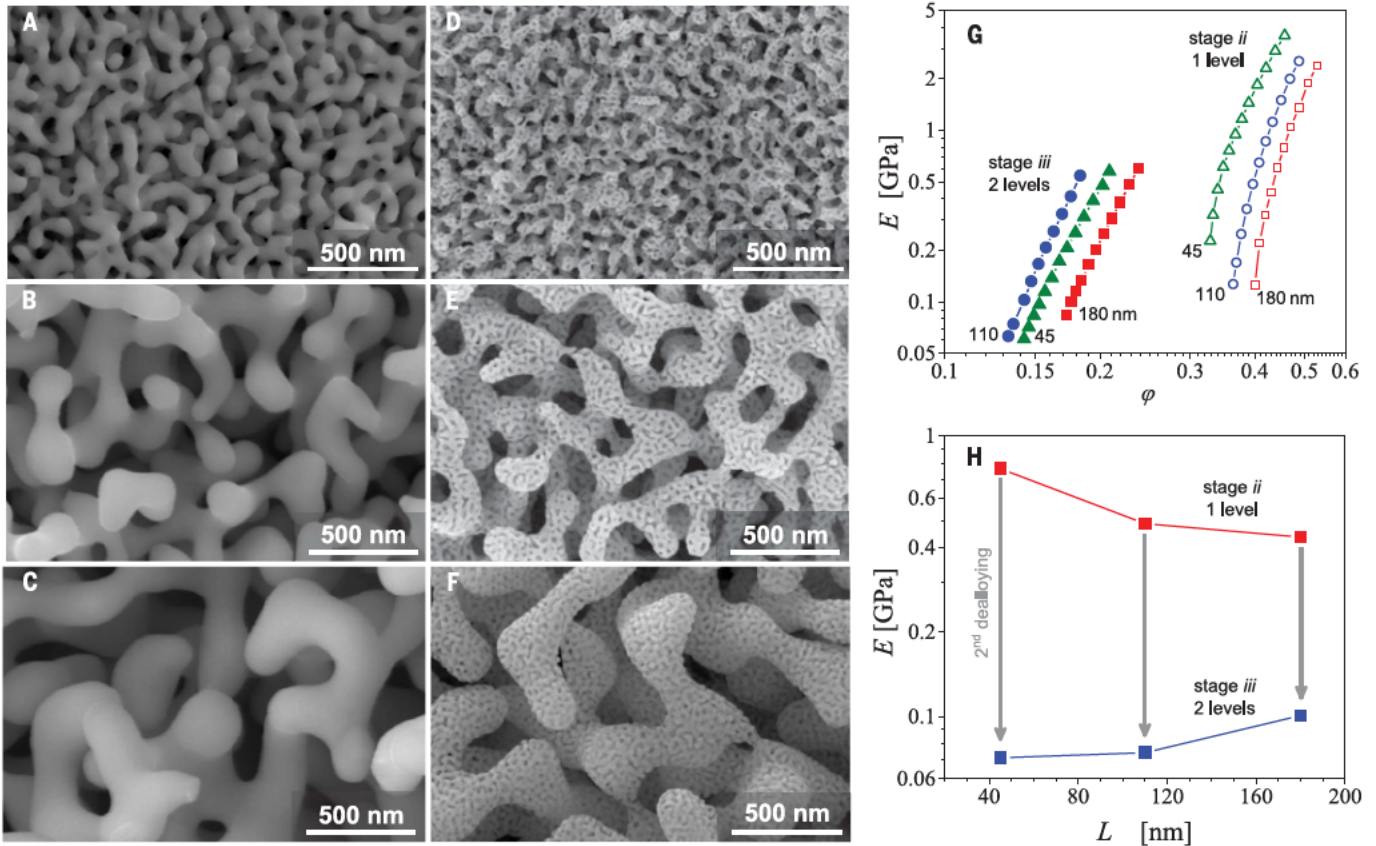


Fig. 4. Size effects on the mechanical performance of N³PG. (A to C) SEM images of stage ii (coarsened nanoporous Ag-Au) samples with different strut sizes: (A) 45 nm, (B) 110 nm, and (C) 180 nm. (D to F) SEM images of stage iii (N³PG) based on the samples in (A) to (C). Strut sizes are similar at the lower hierarchical level, $L_1 = 15$ nm, but different strut sizes exist at the upper hierarchical level, $L_2 = 45$ to 180 nm. (G) Log-log plot of effective Young's

modulus (E) versus solid fraction (ϕ) for stage ii and stage iii samples as in (A) to (F). The value of L_2 is indicated with labels. (H) Log-linear plot of E at 10% compressive strain versus L_2 for samples from (G). The arrows denote the reduction in E between the two states. Relatively higher reduction occurs for smaller L_2 , suggesting a size-dependent elasticity of the struts of the upper hierarchy level.

levels, assuming a strong self-similarity with equal density at each level (Fig. 3). The hierarchical structuring enables load-bearing materials with ϕ below the percolation threshold of the conventional, nonhierarchical material. The hierarchical material is also substantially stiffer and stronger than the nonhierarchical one with the same net ϕ , and this applies particularly near the percolation threshold. This enhanced mechanical behavior at low ϕ is one of the incentives for an interest in structural hierarchy as a pathway to load-bearing, low-density nanoscale network structures.

Comparing the scaling laws with experiment

We compared the model predictions with the experiment, focusing first on the elasticity data (Fig. 3A). We reemphasize the agreement of the literature data for $n = 1$ with the modified Roberts-Garbozci law, specifically including the trend toward a complete disintegration of the material at the percolation threshold (43). Our data show the hierarchical material as load bearing at densities far below that (single-level)

percolation threshold (Fig. 3A). Thereby, its effective E is substantially above that of the nonhierarchical material. With $n = 2$, the scaling law of Eq. 4 overestimates the stiffness of the experimental hierarchical material. Yet the trend for the variation of stiffness with solid fraction is still well reproduced.

The agreement between the model and experiment is even better when it comes to the strength. For nonhierarchical NPG, the scaling law of Eq. 5 with $n = 1$ is in excellent agreement with the experiment. Furthermore, with $n = 2$ the equation almost interpolates the experimental data for the N³PG. The strength of the hierarchical material is systematically and substantially above the scaling law for nonhierarchical NPG, and this observation is well reproduced by our Eq. 5.

Our model does overestimate the stiffness of the experimental hierarchical nanoscale network structures. One obvious conceivable reason is the model's assumption of identical ϕ at each hierarchy level. The material of the experiment may have different ϕ at its two

hierarchy levels, so that its stiffness falls below the prediction. A second, more inherent aspect is that size effects may exist on the mechanical behavior at the upper hierarchy level.

Size effect at upper hierarchical level

Size effects on the strength are well established for metal nanostructures in general (18) and in particular for the struts of NPG (25, 29, 31, 47, 50), which are the elementary structural units at the lowest hierarchy level of our material. By contrast, in NPG the elastic response at that level is essentially size independent (33). Systematic size effects in struts of the higher hierarchy levels of nested-network nanomaterials have not been considered in other experiments.

We started with stage i (as-dealloyed nanoporous Ag-Au) samples with 76 ± 2 at % Ag and $\phi = 0.31$ and prepared a series of stage ii samples with different L by annealing at temperatures between 300° and 500°C. We studied samples with $L = 45, 110,$ and 180 nm (Fig. 4, A to C). Dealloying produced stage iii (N³PG)

samples with $L_1 \approx 15$ nm (Fig. 4, D to F). Consistent with our observation in Fig. 1, C and D, L_2 retains the value of the underlying stage ii material.

We compression-tested two individual samples for each strut size using the same method as previously described. The results are highly consistent (figs. S5 to S7). We determined E versus φ using the unload-and-reload segments (Fig. 2). For the stage ii samples, we found that E at any φ systematically decreases with increasing L (Fig. 4G). As an intrinsic size dependence of the local effective elasticity of the struts can be excluded, we can only explain this trend with a loss of connectivity during the coarsening process by which L is established. This phenomenon has been reported on the basis of experiment (32, 47) and confirmed by numerical simulation (42). Samples with large L made by coarsening are thus expected to have lesser strength and stiffness than as-prepared ones, and the scaling laws based on Eq. 3 will not automatically hold for such samples. Because the second dealloying, leading from stage ii to stage iii, is not expected to substantially change the connectivity at the upper hierarchy level, we expect that the individual stage iii hierarchical samples show different connectivity at their upper hierarchy level, depending on L_2 . This provides for an implicit dependence of the mechanical behavior on the size at the upper hierarchy level.

A second aspect of size dependence emerges from inspection of the data for the stage iii samples (Fig. 4G). Those data do not reflect the size dependence of stage ii one-to-one. Instead, at a given value of φ , the $L_2 = 45$ nm sample is more compliant than the $L_2 = 110$ nm one. Comparing the stiffness values that we computed from the unload-and-reload segments after $\approx 10\%$ strain in the two stages (Fig. 4H) shows that the second dealloying leads to systematically more reduction in E at smaller L_2 . Within the notion that the network connectivity at the upper hierarchy level remains invariant when the lower-level network is generated by the second dealloying, the size-dependent reduction of E implies a size-dependent local value of E of the upper-hierarchy level struts. This observation is not unreasonable, because the “dangling” lower-level struts that end at the surface of upper-level struts can bear no load. This effectively reduces the connectivity of the network at the lower hierarchy level, thereby reducing the stiffness.

Microstructure evolution during deformation

We performed MD simulations of the compression behavior of a computer-generated sample. The microstructural model at each of the two hierarchy levels is based on the leveled-wave model (43), which has been

shown to reproduce $E(\varphi)$ of as-prepared NPG with high precision. We choose $L_2 = 22.6$ nm, $L_1 = 3.0$ nm, and initial $\varphi = 0.125$ (44). The ratio $L_2/L_1 = 7.5$ of the model approximates that (7.3) of the samples underlying Fig. 2. Experimental stress-strain data of a sample with similar ratio and initial solid fraction ($\varphi = 0.119$) are included for comparison (Fig. 5). The simulation and experiment agree with regard to an early onset of plastic yielding, an extended elastic-plastic transition, and a subsequent pronounced strain hardening (Fig. 5, A and B). We plotted stiffness and strength derived from the two data sets against solid fraction (Fig. 5, C and D). Our experiments and simulations are quite consistent and validate our hypothesis that the experimental observations are intrinsically related to the hierarchical structure of the material.

The comparison between cross sections of virtual samples in the plane containing the load axis at strain $\varepsilon = 0$ and 0.29 (Fig. 5A, thick arrows) suggests that the compression is carried predominantly by densification at the upper hierarchy level, whereas the density at the lower hierarchy level varies little.

New contacts are formed upon compression between the struts of the upper hierarchy level (Fig. 5A, thin arrows, and fig. S8). For comparison, we inspect the cross-sectional SEM image of an experimental sample deformed to 55% compressive strain (Fig. 5B). In agreement with the simulation, the SEM image shows that the upper-level struts have been squeezed closer together, whereas at the lower hierarchy level, their internal microstructure remains consistent with that of the undeformed samples.

As a signature of the deformation at the individual hierarchy levels, we investigated the small-angle interference function, S , of the MD-generated model microstructure in various stages of deformation. For the non-deformed microstructure, the graphs of the orientation-averaged (over the full solid angle in reciprocal space) $S(q)$ are dominated by two sharp maxima at the q values of the wave fields used in generating the initial microstructure (Fig. 6A) (here, q denotes the magnitude of the scattering vector). The peak positions measure a mean spacing, \bar{L} , between neighboring struts of the leveled-wave

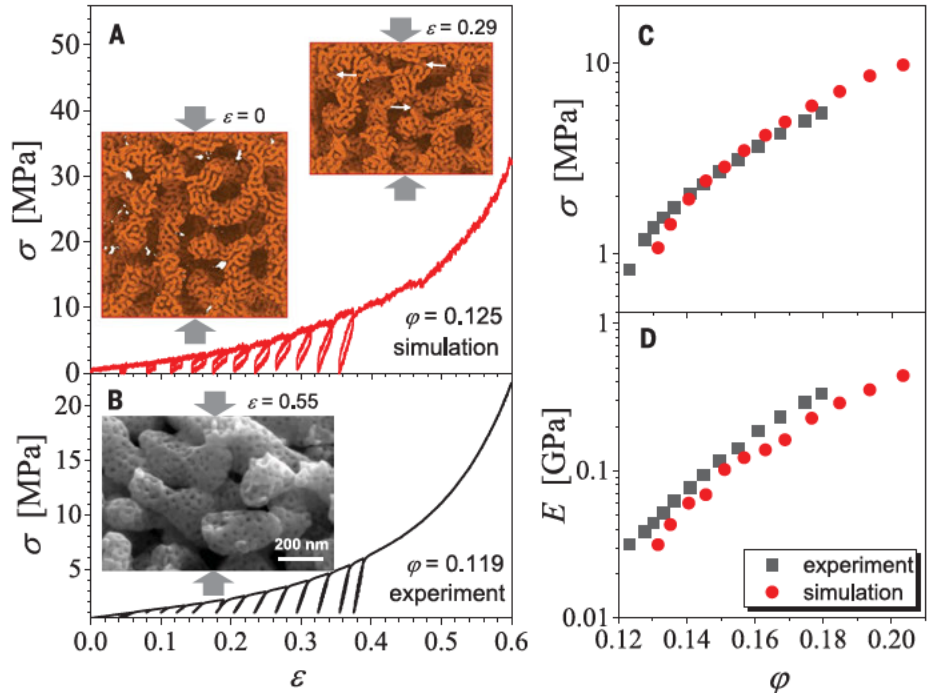


Fig. 5. Comparing experiment and MD simulation of deformation. (A) Compressive engineering stress-strain (σ - ε) curves by MD simulation. (Inset) Microstructure graphs of numerical sample, as relaxed (bottom) and after 29% compression (top). Thick arrows, compression axis; thin arrows, contacts formed during compression. Two well-defined strut sizes are retained. New contacts are formed exclusively at the upper hierarchy level. (B) Compressive stress-strain curves by experiment. (Inset) SEM image of cleavage surface (containing the load axis; arrows) of an experimental sample after 55% compressive strain. Despite high deformation, the two well-defined strut sizes and the high porosity at the lower hierarchy level are retained. (C and D) Evolution of flow stress (σ) and effective Young's modulus (E) versus solid fraction (φ). Data for simulation (red circles) and experiment (black squares) in (C) and (D) are derived from (A) and (B).

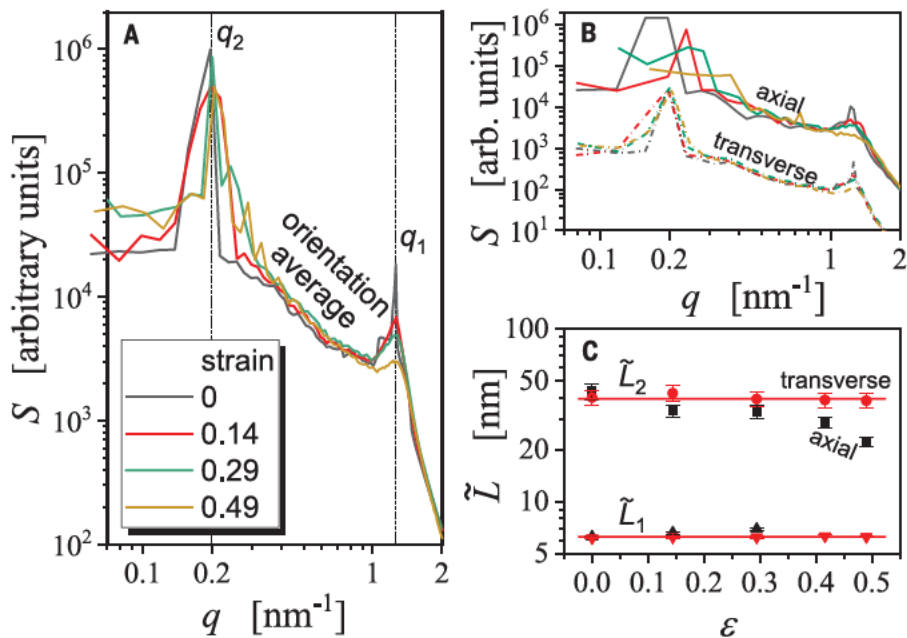


Fig. 6. Variation of small-angle interference function during deformation. (A) Log-log plot of orientation-averaged interference function, S , per atom versus wave vector magnitude, q , for the numerical model structure, unloaded after various engineering strains (legend). Dashed lines: q values of the wave fields generating the network structures of the two hierarchy levels. (B) Log-log plot of $S(q)$, here for $\pm 15^\circ$ sector-averaged S in the direction of the load axis (axial) and in the plane normal to that axis (transverse). Graphs for transverse have been displaced vertically for clarity of presentation. (C) Log-linear plot of characteristic distance (L) between neighboring struts as estimated from peak positions in (B). The distances are shown separately for the lower (L_1) and upper (L_2) hierarchy levels and for the axial and transverse directions. Error bars, q -resolution of the Fourier series underlying the computation of S . Strong compression occurs in the axial direction at the upper hierarchy level.

microstructure as $\tilde{L} = 1.23 \times 2\pi/q$ (43). As the deformation proceeds, the peak at $q = 1.2 \text{ nm}^{-1}$, representative of the lower hierarchy level, broadens but retains its position. This emphasizes that \tilde{L} at that level is conserved, in keeping with the notion (suggested by the real-space structure of the deformed samples) that the lower hierarchy level does not substantially densify (Fig. 5B and fig. S8). The evolution of the peak at $q = 0.20 \text{ nm}^{-1}$, which represents the upper hierarchy level, can be more clearly followed by inspection of direction-resolved interference functions. We computed S separately in the direction of the load axis and in the plane transverse to that axis (Fig. 6B). As the strain increases, the transverse peak remains stationary, whereas the axial one shifts to higher values.

We evaluated \tilde{L} from the peak positions separately for each level and for each direction (Fig. 6C). All strut spacings are essentially conserved during the deformation, with the notable exception of the axial spacing at the upper hierarchy level. That latter spacing decreases from originally 40 to 22 nm at a compressive engineering strain of 0.49. In other words, the direction-resolved interference functions confirm that the densification is pre-

dominantly carried by densification at the upper hierarchy level.

The observation of densification predominantly at the upper hierarchy level reflects the level-dependent loading modes. At the uppermost level, the external load implies uniaxial compression, favoring densification at that level. By contrast, in random networks the struts that contain and form the lower hierarchy levels experience multiaxial loading states with a substantial bending component. Finite-element simulation for random networks similar to NPG supports plastic deformation predominantly in bending (51, 52). Contrary to uniaxial compression, bending does not require densification. This observation is consistent with the low densification at the lower hierarchy level. Our considerations thus suggest that densification predominantly at the upper hierarchy level may be generic for hierarchical network structures loaded in compression. Observations on plastically deformed 2D hierarchical networks (53) appear consistent with that notion.

The upper-hierarchy level struts of N^3PG appear to support ductile plastic bending, whereas NPG is typically brittle when loaded in bending (26). Observations of a tensile

brittle-to-ductile transition in NPG as the ratio R of ligament size to sample size increases to $R \gg 10^{-4}$ (54, 55) suggest an explanation. Because L_2/L_1 is ~ 10 in our samples, the R value of their upper-hierarchy level struts is on the order of 0.1, large enough for ductile behavior.

Summary

We explored the mechanical behavior of nanoscale network materials that are distinguished by a hierarchical structure with self-similar geometry on two distinct length scales. The macroscopic samples, made by dealloying, contained on the order of 10^{12} struts, orders of magnitude more than architected network structures. We suggest that structural hierarchy mitigates the loss in connectivity that can be inherent in nanoscale self-organization processes forming network nanomaterials. Indeed, for a given solid fraction, the stiffness and strength of our hierarchical materials were systematically enhanced as compared with materials with geometrically similar structure but only a single characteristic length scale. Our atomistic numerical simulations support the experiment. Furthermore, we derived scaling laws for the mechanical behavior that embody the impact of hierarchy and that reproduce the experimental trends.

Our findings suggest that, in spite of the self-similarity of the microstructure, the loading modes and the deformation behavior may generally differ between the individual hierarchy levels. The strength of our material is enhanced by its nanoscale struts at the lower hierarchy level, which exploit the established size-dependent strengthening of nanostructures. The data also indicate a size dependence of the mechanics of the upper-hierarchy level struts.

Structural hierarchy can enhance the functional behavior of materials, specifically when it comes to transport phenomena. Our experiments advertise a class of model material for such behavior, and they show that the mechanical properties, which need to be understood irrespective of the material's role as a functional or structural material, are open to informed discussion. Although our experiments used dealloyed Au as the model material, current research generalizes dealloying to lighter, stronger, and less costly metals. This suggests that the approach established in our work offers opportunities for future lightweight nanomaterials with enhanced mechanical behavior at low solid fraction.

REFERENCES AND NOTES

1. C. D. Murray, *Proc. Natl. Acad. Sci. U.S.A.* **12**, 207–214 (1926).
2. D. R. Emerson, K. Cieřlicki, X. Gu, R. W. Barber, *Lab Chip* **6**, 447–454 (2006).
3. P. Trogadas, V. Ramani, P. Strasser, T. F. Fuller, M. O. Coppens, *Angew. Chem. Int. Ed.* **55**, 122–148 (2016).
4. J. Y. Suen, S. Navlakha, *J. R. Soc. Interface* **16**, 20190041 (2019).
5. S. Weiner, H. D. Wagner, *Annu. Rev. Mater. Sci.* **28**, 271–298 (1998).

6. H. Gao, *Int. J. Fract.* **138**, 101–137 (2006).
7. P. Fratzl, R. Weinkamer, *Prog. Mater. Sci.* **52**, 1263–1334 (2007).
8. H. D. Espinosa, J. E. Rim, F. Barthelat, M. J. Buehler, *Prog. Mater. Sci.* **54**, 1059–1100 (2009).
9. E. D. Yilmaz, G. A. Schneider, M. V. Swain, *Philos. Trans. R. Soc. A* **373**, 20140130 (2015).
10. R. Lakes, *Nature* **361**, 511–515 (1993).
11. T. A. Schaedler et al., *Science* **334**, 962–965 (2011).
12. D. Jang, L. R. Meza, F. Greer, J. R. Greer, *Nat. Mater.* **12**, 893–898 (2013).
13. L. R. Meza et al., *Proc. Natl. Acad. Sci. U.S.A.* **112**, 11502–11507 (2015).
14. X. Zheng et al., *Nat. Mater.* **15**, 1100–1106 (2016).
15. J. T. Muth, P. G. Dixon, L. Woish, L. J. Gibson, J. A. Lewis, *Proc. Natl. Acad. Sci. U.S.A.* **114**, 1832–1837 (2017).
16. J. Bauer et al., *Adv. Mater.* **29**, 1701850 (2017).
17. J. R. Greer, V. S. Deshpande, *MRS Bull.* **44**, 750–757 (2019).
18. J. R. Greer, J. T. M. De Hosson, *Prog. Mater. Sci.* **56**, 654–724 (2011).
19. J. J. do Rosário et al., *Adv. Eng. Mater.* **17**, 1420–1424 (2015).
20. A. E. Garcia et al., *Nanoscale Adv.* **1**, 3870–3882 (2019).
21. C. M. Portela et al., *Proc. Natl. Acad. Sci. U.S.A.* **117**, 5686–5693 (2020).
22. X. Y. Yang et al., *Chem. Soc. Rev.* **46**, 481–558 (2017).
23. T. Juárez, J. Biener, J. Weissmüller, A. M. Hodge, *Adv. Eng. Mater.* **19**, 1700389 (2017).
24. J. Erlebacher, M. J. Aziz, A. Karma, N. Dimitrov, K. Sieradzki, *Nature* **410**, 450–453 (2001).
25. H. J. Jin et al., *Acta Mater.* **57**, 2665–2672 (2009).
26. K. Wang et al., *NPG Asia Mater.* **7**, e187 (2015).
27. S. Sun, X. Chen, N. Badwe, K. Sieradzki, *Nat. Mater.* **14**, 894–898 (2015).
28. H. J. Jin et al., *Nano Lett.* **10**, 187–194 (2010).
29. J. Biener et al., *Nano Lett.* **6**, 2379–2382 (2006).
30. C. Volkert, E. Lilleodden, D. Kramer, J. Weissmüller, *Appl. Phys. Lett.* **89**, 061920 (2006).
31. N. J. Briot, T. J. Balk, *Philos. Mag.* **95**, 2955–2973 (2015).
32. N. Mameka, K. Wang, J. Markmann, E. Lilleodden, J. Weissmüller, *Mater. Res. Lett.* **4**, 27–36 (2016).
33. H. J. Jin, J. Weissmüller, D. Farkas, *MRS Bull.* **43**, 35–42 (2018).
34. M. Tsuda, T. Wada, H. Kato, *J. Appl. Phys.* **114**, 113503 (2013).
35. I. V. Okulov et al., *Nano Res.* **11**, 6428–6435 (2018).
36. J. S. Corsi et al., *ACS Sustain. Chem. Eng.* **7**, 11194–11204 (2019).
37. S. H. Joo et al., *Adv. Mater.* **32**, e1906160 (2020).
38. Y. Ding, J. Erlebacher, *J. Am. Chem. Soc.* **125**, 7772–7773 (2003).
39. Z. Qi, J. Weissmüller, *ACS Nano* **7**, 5948–5954 (2013).
40. C. Wang, Q. Chen, *Chem. Mater.* **30**, 3894–3900 (2018).
41. J. Erlebacher, *Phys. Rev. Lett.* **106**, 225504 (2011).
42. Y. Li, B. N. D. Ngò, J. Markmann, J. Weissmüller, *Phys. Rev. Mater.* **3**, 076001 (2019).
43. C. Soyarslan, S. Bargmann, M. Pradas, J. Weissmüller, *Acta Mater.* **149**, 326–340 (2018).
44. Materials and methods are available as supplementary materials.
45. C. Alonso, R. C. Salvarezza, J. Vara, A. J. Arvia, *Electrochim. Acta* **35**, 1331–1336 (1990).
46. D. Artymowicz, J. Erlebacher, R. Newman, *Philos. Mag.* **89**, 1663–1693 (2009).
47. L. Z. Liu, X. L. Ye, H. J. Jin, *Acta Mater.* **118**, 77–87 (2016).
48. L. J. Gibson, M. F. Ashby, *Cellular Solids: Structure and Properties* (Cambridge Univ. Press, 1999).
49. Y. H. Xiang, L. Z. Liu, J. C. Shao, H. J. Jin, *Acta Mater.* **186**, 105–115 (2020).
50. A. Hodge et al., *Acta Mater.* **55**, 1343–1349 (2007).
51. N. Huber, R. N. Viswanath, N. Mameka, J. Markmann, J. Weissmüller, *Acta Mater.* **67**, 252–265 (2014).
52. M. T. Hsieh, B. Endo, Y. Zhang, J. Bauer, L. Valdevit, *J. Mech. Phys. Solids* **125**, 401–419 (2019).
53. D. Mousanezhad et al., *Sci. Rep.* **5**, 18306 (2015).
54. R. Li, K. Sieradzki, *Phys. Rev. Lett.* **68**, 1168–1171 (1992).
55. N. Badwe, X. Chen, K. Sieradzki, *Acta Mater.* **129**, 251–258 (2017).

ACKNOWLEDGMENTS

Funding: This work was supported by Deutsche Forschungsgemeinschaft (Projektnummer 192346071 SFB 986). The authors gratefully acknowledge U. Dette for her assistance with sample preparation. **Author contributions:** S.S. and J.W. designed the experiments and the theory. S.S. performed the experiments. Y.L. performed the simulation. All authors participated in analysis, discussion, and manuscript writing. **Competing interests:** The authors declare no competing interests. **Data and materials availability:** All data needed to evaluate the conclusions in the paper are presented in the main text or the supplementary materials.